

Explaining Cu@Pt Bimetallic Nanoparticles Activity Based on NO Adsorption

Francesc Viñes*^[a,b] and Andreas Görling^[a,c]

Abstract: Cu@Pt nanoparticles (NPs) are experimentally regarded as improved catalysts for the NO_x storage-reduction, with higher activities and selectivities compared to pure Pt or Cu NPs, and to inverse Pt@Cu NPs. Here, a density-functional theory based study on such NP models with different sizes and shapes reveals that the observed enhanced stability of Cu@Pt compared to Pt@Cu NPs is due energetic reasons. On both types of core@shell NPs charge is transferred from Cu to Pt, strengthening the NP cohesion energy in Pt@Cu NPs, and spreading charge along the surface in Cu@Pt NPs. The negative surface Pt atoms in the latter diminish the NO bonding due to an energetic rise of the Pt bands, as detected by the appliance of the *d*-band model, although other factors such as atomic low coordination or the presence of an immediate subsurface Pt atom do as well. A charge density difference analysis discloses a donation/backdonation mechanism in the NO adsorption.

Keywords

Core@shell Nanoparticles • NO adsorption • Bimetallic CuPt • Electronic Structure • Density Functional Calculations

[a] *Dr. Francesc Viñes, Prof. Dr. Andreas Görling*

Lehrstuhl für Theoretische Chemie, Friedrich-Alexander-Universität Erlangen-Nürnberg, Egerlandstraße 3, Erlangen, D-91058, Germany.

[b] *Prof. Francesc Viñes*

Departament de Ciència de Materials i Química Física & Institut de Química Teòrica i Computacional (IQTCUB), Universitat de Barcelona, c/ Martí i Franquès 1, Barcelona 08028, Spain

E-mail: francesc.vines@ub.edu

[c] *Prof. Dr. Andreas Görling*

Erlangen Center for Interface Research and Catalysis, Friedrich-Alexander-Universität Erlangen-Nürnberg, Egerlandstraße 3, Erlangen, D-91058, Germany

1. Introduction

Metal nanoparticles (*NPs*), aggregates containing dozens up to many millions of atoms, have become a hub of research,^[1] given that their properties are framed in between those of individual metal atoms and bulk metals. Such properties normally display a size dependency evolution which allows their tuning,^[2] where two clear regions of size dependency are normally encountered; either with properties being scalable towards the bulk limit or not. The latter is the so-called non-scalable regime, found at very small sizes, where each atom counts in defining the property value, and, therefore, with no clear trend towards the bulk limit.^[3] It is particularly in this latter region where quantum size effects on the NPs activity are more relevant, although one should not forget the key role played by the ratio in between atoms located at the surface of the nanoparticle, having low Coordination Numbers (*CNs*), with respect to those in the bulk, being fully coordinated. The low CN of metal atoms at NP edges and corners is normally responsible of the observed enhanced activity to attach molecules,^[4] although the lack of coordination also enables a larger flexibility which further helps at better accommodating the adsorbed species. All these aspects are known not to merely affect a metal NP chemical activity, but also its reactivity performance towards heterogeneously catalysed processes carried on the NP exposed surfaces, up to the point of being a possible key point in the catalytic selectivity.^[1,5,6]

In addition to monometallic NPs, metal alloys are in widespread use in heterogeneous catalysis, where the constituent metallic atoms and their proportion further define the bimetallic NPs chemistry,^[1,2] offering in addition to a variation of the particle size a second level of tuning. To date the modelling of such bimetallic NPs is a tremendous challenge, specially when tackling size, shape, and composition components, although steps forward have been achieved by the breakdown of different energy contributions from distinct topological regions.^[7] From these studies, one frequently observes an energetic preference towards various core@shell architectures,^[2,7] by that, simplifying the possible atomic arrangements, as one would need to regard only the core and shell atomic compositions so as to increase/decrease the surface electron density, ultimately modifying the NP surface chemical properties.^[8] Because of this, core@shell structures have been extensively investigated as a way of accessing unique physicochemical properties, not feasible in one material alone.^[9] As a result, the synthesis of core@shell NPs has attracted a great deal of interest with potential applications not only restricted to catalysis, but also appealing in

semiconductor engineering, magnetic composites, drug delivery, enzyme immobilization, molecular recognition, and chemical sensing, to name a few other fields of applicability.^[2,10]

One particularly interesting system is that of bimetallic CuPt NPs. The first synthesis of colloidal CuPt nanoparticles, reported by Toshima and Wang, revealed their possible catalytic use in hydrogenation reactions in solution.^[11] More recently, CuPt alloys have been suggested to efficiently catalyse the NO_x reduction,^[12] a technologically relevant reaction for exhaust gases treatments.^[13] Usually, the synthesis impregnation methods make it difficult to identify and evaluate the actual catalytic species, although in order to fully understand the catalytic activity of CuPt bimetallic NPs, a comparison of their activities with respect to monometallic NPs at an atomistic level of understanding is essential to foster further advances, specially when carried out as a function of NP size, shape, and composition.

Such a detailed knowledge can be approached combining sophisticated experimental techniques, as done, *e.g.* by Zhou and coworkers.^[14] These authors experimentally investigated, in a systematic fashion, the synthesis, stability, and characterization of monometallic Cu and Pt NPs, and bimetallic CuPt NPs, including Cu@Pt and inverse Pt@Cu core@shell NP systems. Transmission Electron Microscopy (*TEM*), X-Ray Diffraction (*XRD*), and Energy Dispersive X-ray (*EDX*) spectroscopy studies were used to characterize such NPs, with diameters, \emptyset , ranging 4-20 nm, while all NPs maintained a face-centred cubic (*fcc*) crystallographic structure. The XRD studies showed that Pt@Cu NPs had a Pt core with a Pt_{0.2}Cu_{0.8} Cu-rich alloy shell. However, annealing at 360 °C converted these NPs into a CuPt alloy. In contrast, the annealing on Cu@Pt NPs led to no CuPt alloy but rather to a more Cu-rich core. This different behaviour was attributed to the greater kinetic stability of Cu@Pt NPs, in principle, controlled by the Kinkendall mass-transport phenomenon, which has its origin in the different atomic diffusion of Cu or Pt atoms into the Pt or Cu bulk matrix systems, respectively.^[15]

The catalytic performance of the aforementioned systems was evaluated in the reduction of NO using H₂ as a reducing agent, being one of the reactions taking place in the NO_x Storage-Reduction (*NSR*) catalyst,^[16] with the ultimate goal of having high degrees of conversion while being selectively addressed towards the N₂ product. Pt NPs are typically used as active phases in NSR,^[16,17] with very high activities and essentially a complete NO conversion. However, they display certain drawbacks, including *i*) a low selectivity towards N₂ species, *ii*) susceptibility towards sulphur poisoning due to the competitive adsorption of SO_x species and/or their perturbation effect on the Pt electronic structure,^[17-19] and *iii*) the

high cost of the precious Pt. Quite interestingly, the Cu@Pt NPs maintain the high reactivity of Pt NPs with a much better N₂ selectivity, up to 93%, while being stable under the catalytic working temperature of 360 °C. In contrast, Pt@Cu NPs showed very little NO conversion, *a priori*, due to the Cu-rich shell structure, and the N₂ selectivity was found to drop over time until meeting that of CuPt alloy.^[14]

However, the reasons for the enhancement of the Cu@Pt catalytic power and the degradation of Pt@Cu NPs in the course of NO reduction remain hitherto undisclosed. In this context possible near surface alloy effects are relevant insomuch that the subsurface metal or alloy layers affect the binding of adsorbates and, ultimately, the reaction rate and selectivity.^[20] Here this still open question is addressed, gaining the necessary atomic knowledge by simulations based on Density-Functional Theory (*DFT*). Both Pt and Cu NPs reference models, as well bimetallic core@shell Cu@Pt and Pt@Cu NP ones have been considered, exploring NO adsorption as a probe related to NSR. Suitable NP models are built up with the aim of going well-beyond the non-scalable regime region,^[3] where core regions might be still excessively small so as to mimic larger sizes of NPs.^[21] Different sizes and shapes are scrutinized, so as to disclose geometric or size effects which might influence the different NO adsorption behaviours.

2. Results and Discussion

2.1. Monometallic NPs

As a first step, the evolution with size of structural and energetic properties of the Cu and Pt NPs has been investigated, in order to ascertain the scalability of such properties, following procedures already described in the literature.^[3,22,23] Thus, the mean cohesive energy per atom, E_{coh} , has been gained for each cluster and NP, and calculated as

$$E_{coh} = (E_{M_n} - nE_M)/n \quad (2),$$

where E_{M_n} is the energy of the optimized metal cluster or NP (M = Cu or Pt) with n atoms, and E_M the energy of an isolated Cu or Pt atom in the vacuum. Within this definition, the more negative the E_{coh} , the more stable the M_n system is. Apart from E_{coh} , the mean shortest interatomic distance, $d(M-M)$, has been obtained for the optimized M_n systems. The optimization and model details are described in the Computational Details section. The evolution of these two quantities with the cluster or NP size has been evaluated with respect to $n^{-1/3}$, as successfully carried out in the past,^[22,23] used as an approximation to the mean particle radius $r^{-1} \sim n^{-1/3}$. Thus, the bulk limit is given by $r^{-1} = 0$.

The scalability trends are shown in Figure 1. From them, the higher stability of Pt NPs compared to Cu NPs is easily revealed, showing smaller E_{coh} values for the latter case. Further than that one notices the shorter intermetallic distances of Cu, with its atomic radius being smaller than that of Pt, and, more importantly, the monotonic linear trends of E_{coh} and $d(M-M)$ towards the bulk limits. Indeed, the linear trends are excellent; for E_{coh} , the gained equations, being $E_{coh}^{Cu} = 2.98 \cdot n^{-1/3} - 3.56$ for Cu and $E_{coh}^{Pt} = 4.31 \cdot n^{-1/3} - 6.00$ for Pt, display regression coefficient values, R , of 0.989 and 0.977, respectively, evidencing the linear dependency of such properties with size. Furthermore, the intersects at bulk limits imply E_{coh} values of -3.56 and -6.00 eV·atom⁻¹, which are only ~0.1 eV·atom⁻¹ away from bulk calculated E_{coh} values of -3.48 and -5.90 eV·atom⁻¹, respectively, and thus, within the standard DFT accuracy of ~0.1-0.2 eV. The linear equations for $d(M-M)$ are also excellent, being $d(Cu-Cu) = -0.26 \cdot n^{-1/3} + 2.58$ and $d(Pt-Pt) = -0.32 \cdot n^{-1/3} + 2.83$ for Cu and Pt, respectively, with R values of 0.959 and 0.958, respectively, with their intersects at 2.58 and 2.83 Å differing solely by 0.01 Å from the PBE optimized bulk values of 2.57 and 2.82 Å, respectively.

In general terms such tendencies are well understood, in the sense that E_{coh} decreases when the NPs size decreases. In such situations, the high proportion of metal atoms at the NP facets, edges, and corners implies having such atoms undercoordinated compared to bulk situations, and by that, being more unstable, a fact translated in a smaller E_{coh} . Furthermore, the $d(M-M)$ distances decrease when having smaller NP; the origin of such phenomenon is the same. The lack of coordination prompts a mechanism of bond compensation, strengthening the bonds to the remaining neighbouring atoms. This is translated into a small shrinking of the NPs volume, and the overall lower mean $d(M-M)$ values.

A further analysis can be made when distinguishing between different shapes, so as to ascertain whether a certain shape is more stable than others at certain cluster or NP sizes. The evolution with respect to $n^{-1/3}$ has been evaluated for Cu_n and Pt_n NPs according to the four types of shapes here contemplated; octahedral, cuboctahedral, icosahedral, and spherical-like. Excellent linear trends are found for each case, as shown in Figure 2, with slight variation in slopes, a , and intercepts, b , see Table 1, but in all cases with excellent regression coefficients, R , well above 0.992. Clearly, the linear size evolution displayed in Figure 1 suffers from little dispersion of values due to the mixing of different shapes, which results in slight deviations from the linear behaviour with respect to $n^{-1/3}$. In any case, the NPs stabilities are scattered over a ~0.1-0.2 eV range. Notice, that the Cu_n intercepts are in between -3.53 and -3.69 eV,

thus, within the DFT accuracy regarding the bulk value of -3.56 eV. In the case of Pt_n NPs, the obtained intercepts range -5.94 to -6.21 eV, still, with a very good agreement with bulk value of -5.9 eV.

As far as shapes are concerned, for very small particles —large $n^{-1/3}$ values— octahedral shapes are preferred, even though this goes against to the predicted Wulff shapes of stability, which point for cuboctahedral shapes being the most stable ones,^[34,40] highlighting that, at these sizes, edge and corner energies are playing a determining role well beyond surface/facet energies, being these latter the only ones determining the Wulff shapes of stability.^[3] For Pt NPs, the (Wulff predicted) cuboctahedral shapes becomes the preferred ones for $n = 236$ atoms onwards, which would correspond to an approximated diameter of $\varnothing \sim 1.9$ nm, considering the n Pt atoms as spheres with a radius given by half the mean $d(\text{Pt-Pt})$ distance, gained at this n size from the linear regression shown in Figure 1. This crossing thus defines the size from which the Wulff shapes of stability can be safely applied on. However, Cu NPs behave different. Here, apparently, the crossing point is towards icosahedral particles, at $n \sim 55$ atoms. Indeed, the icosahedral NP shape is known to be the energetic minimum for Cu₅₅, as observed both experimentally^[24] and theoretically.^[25] However, this cluster size appears to be a magic cluster of stability, and, actually, its combination with the modest stability of the Cu₁₃ cluster bias the shape evolution trend with size. A closer inspection of the points in Figure 2 reveals a change of trend from Cu₅₅ onwards. The linear trend on this subset of icosahedral shapes, and therefore, neglecting the Cu₁₃ icosahedron, would imply a crossing point towards cuboctahedral structures for $n = 239$ atoms, with a $\varnothing \sim 1.7$ nm, thus, similar to the crossing point found for Pt NPs. According to this analysis, the Cu@Pt and Pt@Cu NPs used in NSR, with \varnothing ranging from 4 to 20 nm, would be better modelled with Wulff-shaped cuboctahedral NPs.

2.2. Bimetallic NPs

After examining the monometallic Pt and Cu NPs stability by means of their mean E_{coh} , it is necessary to assess the stability of bimetallic Pt@Cu and Cu@Pt core@shell model structures, described in the Computational Details. On a first step the excess energy per metal atom, E_{exc} , has been acquired, defined for Pt@Cu NP cases as

$$E_{exc}(Pt_i@Cu_j) = \left(E(Pt_i@Cu_j) - \frac{i}{n}E(Pt_{i+j}) - \frac{j}{n}E(Cu_{i+j}) \right) \cdot \frac{1}{n} \quad (3),$$

where $E(Pt_i@Cu_j)$ is the total energy of a given bimetallic system, having a total number of atoms, $n = i + j$. Thus, the $E(Pt_n)$ and $E(Cu_n)$ are the total energies of monometallic Pt_n and Cu_n respectively. With this definition, a negative value of E_{exc} implies a release of energy. This implies that the mixing and formation of a bimetallic NP over the respective monometallic NPs is favourable for the considered size and shape. Note in passing by that the same equation can be used to formulate the excess energy for Cu@Pt NPs.

The E_{exc} values for Pt@Cu and Cu@Pt NPs are encompassed in Table 2, alongside with the NP average Pt-Pt, Cu-Cu, and Pt-Cu nearest neighbor distances, $d(Pt-Pt)$, $d(Cu-Cu)$, and $d(Cu-Pt)$, respectively. Regardless of the structures, the excess energies are all negative, showing a preference towards mixing, and therefore, indicating that segregation would be prevented in such bimetallic NPs. Further than that, Cu@Pt NPs display E_{exc} values in between -79 and -299 meV, thus, much more stable than the respective values for Pt@Cu NPs, ranging -37 and -141 meV, which is a clear sign of the higher stability of Cu@Pt core@shell NPs. This result agrees perfectly with the aforementioned experiments, in which Pt@Cu NPs are found to evolve towards a CuPt alloy when annealing, whereas Cu@Pt NPs better maintain their core@shell structure, thus pointing to Cu@Pt NPs as being more stable than Pt@Cu ones.^[14] At variance with the work of Zhou *et al.*, however, the different behaviour of Cu@Pt and Pt@Cu NPs is explained from a thermodynamic stability point of view, and, therefore, not due to a kinetic stability in its origin.

Focusing on the average interatomic distances, one immediately sees that for Pt@Cu NPs the $d(Pt-Pt)$ range 2.78-2.80 Å, therefore, very close to the bulk Pt value of 2.81 Å, revealing a similar geometric environment of the Pt core. The same occurs for $d(Cu-Cu)$ in Cu@Pt NPs that exhibits interatomic distances in the range of 2.56-2.60 Å, which is close to the Cu bulk interatomic distance of 2.57 Å. The actual differences are found indeed for the NP shell, and its contact to the NP core. In the case of Cu@Pt NPs, the Pt shell shows $d(Pt-Pt)$ distances of 2.66-2.69 Å, much smaller than on the equivalent in size Pt_n NPs, see Figure 1, which could be regarded as an indicator of an enhanced chemical activity, yet they are not, see below. Further than that, the bonds between the Pt core and the Cu shell range from 2.69 to 2.74 Å, revealing a strong attachment in between the two phases. However, for Pt@Cu NPs, the shell $d(Cu-Cu)$, ranging 2.59-2.76 Å, are larger than the corresponding values for Cu_n NPs, see Figure 1. Moreover, the bonding of surface Cu atoms to the Pt shell, as shown by $d(Cu-Pt)$, are fringed in between 2.59 and 2.63 Å, in average terms, shorter than Cu-Cu shell bonds, and so, these results point for Cu-Pt bonds being stronger than Cu-Cu ones.

A further analysis can be made by computing the bimetallic cohesive energies, here defined as

$$E_{coh} = (E_{Pt_iCu_j} - iE_{Pt} - jE_{Cu})/n \quad (3).$$

The evolution of the computed bimetallic E_{coh} with respect to $n^{-1/3}$ is shown in Figure 3, with the distinction for the different considered NP shapes. One immediately notices that, overall, Pt@Cu NPs are systematically less stable than Cu@Pt NPs, thus adding up for the energetic stability of the latter under working conditions. Furthermore, the instability of Pt@Cu NPs seems to be more pronounced for small NPs, given the reduction of E_{coh} when increasing $n^{-1/3}$, independently of the shape. However, the stability approach of Pt@Cu NPs towards Cu@Pt ones explain their synthesizability, although their higher energy makes their conversion into either a CuPt alloy, or even a Cu@Pt unavoidable under working operando conditons. The stability of Cu@Pt does not seem to be much affected by size, as it stays essentially constant with $n^{-1/3}$. Even though the explored NP systems are a few, it seems as cuboctahedral shapes are normally preferred for Cu@Pt NPs, especially for large sizes, which further supports considering cuboctahedral NPs as suitable computational models. In the case of Pt@Cu NPs, all sorts of shapes seems to be feasible, and only octahedral shapes seem to be somewhat disfavoured.

In addition to the energetic stability and geometric analysis, the possible charge transfer within the NPs has been studied. A Bader charge analysis^[26] on the electron density of all the considered systems is shown in Table 3. In both sets of Pt@Cu and Cu@Pt NPs there is electron density charge transferred from Cu to Pt, resulting in a negatively charged Pt core and positively charged Cu shell in the Pt@Cu NP systems, and the negative image is found for Cu@Pt NPs. From the results shown in Table 3 the total amount of transferred charge naturally grows with size with no apparent shape effect, although there are variations as per type of metal and location. On Pt@Cu NPs the shell Cu atoms charge is kept essentially constant, being $\sim 0.1 e$, while being $\sim -0.1 e$ for shell Pt atoms in Cu@Pt NPs, see Figure 4. On the contrary, the charge per core Cu does slightly change with $n^{-1/3}$, getting linearly reduced for larger Cu@Pt NPs with a linear equations of $Q_{Cu} = 1.24 \cdot n^{-1/3} - 0.04$ and $R = 0.9461$, yet the opposite occurs for Pt@Cu NPs, where the negative charge of core Pt reduces with NP increasing size as $Q_{Pt} = -1.16 \cdot n^{-1/3} + 0.05$ and $R = 0.9702$. Thus, the size effect seems to be related to the core region, possibly biased by the electronic confinement.

Considering the charge transfer within the bimetallic core@shell systems, a question arises on whether the charge accumulates on certain regions or it is evenly distributed within the particle otherwise. To investigate this problem the so-called Charge Density Difference (CDD) analysis has been carried out for two Wulff-shaped model systems within the scalable regime, Pt₄₄@Cu₉₆ and Cu₄₄@Pt₉₆, see Figure 5. A closer look at the CDD plot of Pt₄₄@Cu₉₆ leads to the conclusion that the charge is being transferred from *d* orbitals of the Cu shell atoms to the core@shell interface as well as to Pt core *d* orbitals, accompanied to some extent by some Pt core charge redistribution towards the core@shell interface. This picture is consistent with the aforementioned short *d*(Cu-Pt) bond, implying a rather strong bond. For Cu@Pt systems one would expect a similar behaviour, but, according to Figure 5, less pronounced charge differences show up, up to the point of displaying Pt shell electronic depletion. This surprising feature appears to imply more a charge redistribution within the layers, where electron density is removed from the d_z^2 orbitals of Pt atoms central of the (111) facet atoms and spread along the facet, a point that might diminish the NO adsorption behaviour on these facets, see below.

2.3. NO Adsorption on Monometallic NPs

After describing the Cu_{*n*}, Pt_{*n*}, and Cu@Pt and Pt@Cu NP models, we study NO adsorption on them, evaluating energetic, structural, and charge distribution aspects. Firstly, as a reference, the adsorption of NO on Cu_{*n*} and Pt_{*n*} NPs, on the (111) facets most central face-centred cubic (*fcc*) and hexagonal close-packed (*hcp*) three-fold hollow sites is assessed, representing the vast majority of sites in large NPs, as the ones of $\varnothing \sim 4\text{--}20$ nm as in the experiments,^[14] see more explanations in the Computational Details. Similar three-fold hollow sites are evaluated on icosahedral NPs as well, in the middle of the (111)-like facets. In all cases, the NO adsorbs on these three-fold hollow sites coordinated by the N atom, with the O pointing perpendicular to the (111) or (111)-like facet. Table 4 displays the computed E_{ads} , alongside with the reference values of *fcc* and *hcp* sites of Cu and Pt (111) surface slab models, including geometric aspects, such as the molecular NO bond length, $d(\text{N-O})$, the height h of the N atom to the (111) surface plane, and the mean distances $d(\text{N-Cu})$ and $d(\text{N-Pt})$ of N to each of the three Cu or Pt atoms, respectively, which define the three-fold hollow site where the NO molecule is adsorbed. The mean distances between these Cu and Pt surface atoms, $d(\text{Cu-Cu})$ and $d(\text{Pt-Pt})$, are also listed.

An inspection of the values in Table 4 reveals that for the Pt_{*n*} NPs E_{ads} between -164 kJ·mol⁻¹ (Pt₁₄₆) and -225 kJ·mol⁻¹ (Pt₃₀₉) are found. The strongest adsorption energies are

found for icosahedral NPs with $-203 \text{ kJ}\cdot\text{mol}^{-1}$ for Pt_{147} and $-225 \text{ kJ}\cdot\text{mol}^{-1}$ for Pt_{309} . On Pt_{147} the bonds between the Pt atoms that constitute the three-fold hollow site where NO adsorbs are elongated by 0.1 \AA compared to the Pt_{309} case, also increasing the $d(\text{N-Pt})$ bonds by 0.03 \AA and the NO molecule being closer to the NP by 0.04 \AA , in accordance to the stronger bond. The weakest adsorptions are encountered for *hcp* hollow sites on small octahedral (Pt_{146}) and cuboctahedral (Pt_{140}) NPs, with E_{ads} values of -164 and $-170 \text{ kJ}\cdot\text{mol}^{-1}$. For the rest of NPs sizes, shapes, and sites, the adsorption strengths are comparable to the extended (111) surface limits of $180\text{-}200 \text{ kJ}\cdot\text{mol}^{-1}$. The difference of $14 \text{ kJ}\cdot\text{mol}^{-1}$ in between *hcp* and *fcc* sites of the Pt (111) slab model is explained based on the Pt atoms size, which implies more steric repulsion for the *hcp* hollow site, having one Pt atom of the second layer directly underneath.

It is worth to notice the small E_{ads} of $170 \text{ kJ}\cdot\text{mol}^{-1}$ in the cuboctahedral Pt_{140} NP, whereas other smaller and larger NPs with the same shape display larger E_{ads} values, see Table 4. By having a look at the geometric data one does not find a reason for this weaker attachment. Regardless of this, one can detect that the NO adsorption is stronger on those cuboctahedral particles that display larger (001) facets, these are, Pt_{116} and Pt_{201} , compared to those with small (001) facets, *i.e.* Pt_{140} and Pt_{225} . Actually, the latter E_{ads} nicely compare to octahedral Pt_{146} and Pt_{231} NPs displaying no (001) facets. This concludes that lower E_{ads} for Pt_{140} arises from geometry and size effects from second Pt neighbors. For instance, on Pt_{116} such second Pt neighbors are located at NP low-coordinated edge sites, whereas in Pt_{140} they are within the (111) facet. Therefore, on Pt_{116} , such undercoordinated second-neighbor Pt atoms display a higher activity, and so contribute in attaching the NO molecule, being responsible of the difference in E_{ads} on the same *hcp* type of hollow. Furthermore, such Pt atoms at edges display a larger capability to accommodate species upon, even allowing space for the first Pt neighbors relaxation. Altogether, such coordination and capability factors are responsible of strengthening the adsorption of NO, as observed in the past for the adsorption of C adatoms and NO molecules on the similar systems of Pd NPs,^[27,28] and also nowadays regarded as the effect of the generalized coordination number. This is, not only the Coordination Number, CN —the number of first neighboring metal atoms— of the surface metal atoms involved in the NO attachment defines the NO adsorption strength, but this bonding is also affected by the CN of the surface metals second neighbors, an effect quantified through the generalized CN, $\overline{\text{CN}}$, for whose detailed definition we refer to the literature.^[29] Accordingly, this explanation also applies on the enhanced E_{ads} of $-203 \text{ kJ}\cdot\text{mol}^{-1}$ observed on the small Pt_{135} spherical NP compared to the larger Pt_{260} one.

As far as Cu_n NPs are concerned, the weakest E_{ads} of $-141 \text{ kJ}\cdot\text{mol}^{-1}$ is found for Cu_{140} , whereas the strongest is displayed again for Cu_{309} icosahedral structure, with a value of $-247 \text{ kJ}\cdot\text{mol}^{-1}$. At variance with Pt_n NPs, and with the sole exception of Cu_{140} , all the studied cases yield E_{ads} values larger than the equivalent sites for the (111) extended surface, being $-140 \text{ kJ}\cdot\text{mol}^{-1}$ and $-143 \text{ kJ}\cdot\text{mol}^{-1}$ for *fcc* and *hcp* hollow sites, respectively. Consequently, it seems that NO adsorption gets favored when nanostructuring Cu. This can even lead to changes of the NO adsorption preference, this is, by comparing NO E_{ads} on Cu_n and Pt_n NPs one finds that, depending on the shape and size, the NO adsorption can be preferred on Pt or Cu, e.g. for the cuboctahedral particles the Pt NPs show a slightly stronger adsorption than the Cu NPs, whereas the inverse trend is found for the octahedral NPs. The very low E_{ads} for cuboctahedral Cu_{140} can be explained based on the flexibility and $\overline{\text{CN}}$ effects, as above discussed for the Pt_{140} case. Nevertheless, in mean terms, there seems to be a stronger bonding on Pt_n compared to Cu_n , by about $14 \text{ kJ}\cdot\text{mol}^{-1}$ in average. This goes along with a reported slightly higher *d*-band center, ϵ_d , of bulk Pt, -2.73 eV , compared to bulk Cu, of -2.86 eV , as obtained in previous DFT PBE estimates carried out on the same computational set up grounds,^[30] and implying, in general, higher energy Pt bands, more prone to bind molecular moieties with a larger strength. This ϵ_d difference is even more pronounced when dealing with (111) surfaces, with estimates of -2.16 and -2.56 eV for Pt and Cu, respectively, further supporting the here observed higher chemical activity of Pt surfaces.^[31]

The bonding of NO to the Cu_n and Pt_n NPs has been analyzed as well in terms of charge transfer and charge redistribution. Table 5 shows the Bader charges Q_{Pt} and Q_{Cu} of the Pt and Cu NPs, respectively, and that of the adsorbed molecule, Q_{NO} . In all cases, charge is transferred from NPs to the adsorbed NO. For Pt NPs this is $\sim 0.5 e$, whereas $\sim 0.6 e$ are transferred for Cu NPs. The slightly larger charge transfer from Cu NPs goes along with the slightly larger NO E_{ads} , suggesting that the system capability on supplying charge to the NO could be a factor that could strengthen the NO adsorption. The electronic transfer is towards the $2\pi^*$ antibonding orbital of NO, which reduces its bond order and induces a N-O bond elongation, as seen by $d(\text{N-O})$ distances of 1.22 - 1.23 \AA for Cu NPs and 1.21 - 1.22 \AA for Pt NPs, see Table 4, elongated from a computed value of 1.17 \AA for the isolated NO molecule.^[27]

The charge transfer has been evaluated as well with CDD analyses, exemplified for Pt_{140} and Cu_{140} cases in Figure 6, and showing, for clarity, only the NO molecule with the three surface metal atoms plus the metal atom of the second layer lying right underneath the

NO molecule, given that for Pt₁₄₀ and Cu₁₄₀ NPs NO is adsorbed on an *hcp* hollow site. In both cases charge transfer and redistribution are observed. The d_z^2 orbitals of the involved metal hollow atoms show a clear depletion. However, in Pt₁₄₀, the subsurface Pt receives part of this charge in a d_z^2 orbital whereas this does not happen for Cu₁₄₀, revealing how subsurface Pt atoms are involved in the NO binding. Similar results are found for *fcc* sites, except for the involvement of the subsurface Pt. For Pt₁₄₀ the adsorbed NO molecule experiences electron depletion from the 2σ orbital, indicated by the globes over N and O atoms. Besides, there is electron accumulation in d_{xz} and d_{yz} character Pt orbitals as well as in the aforementioned $2\pi^*$ orbital of NO. The full picture is thus consistent with a donation/backdonation bonding mechanism. For Cu₁₄₀ the situation is quite resembling, with the only caveat of missing the electron accumulation in the d_{xz} and d_{yz} orbitals of the three Cu atoms, plus that the underlying Cu atom is neither involved in any charge transfer nor rearrangement.

2.4. NO Adsorption on Bimetallic NPs

Finally, the NO molecule has been adsorbed on exactly the same sites as the aforementioned Cu_{*n*} and Pt_{*n*} NP reference models, but now contemplated on the Cu@Pt and Pt@Cu core@shell NP systems. The adsorptive and geometric results are listed in Table 6. For the Pt@Cu NPs the E_{ads} range between -142 kJ·mol⁻¹ (Pt₄₄@Cu₁₀₂) and -181 kJ·mol⁻¹ (Pt₁₁₆@Cu₁₁₄). In the particular case of the spherical-like Pt₄₃@Cu₉₂ NP and the icosahedral like Pt₁₄₇@Cu₁₆₂, the E_{ads} belong to bridging configurations; at the NP edge in the former or within the (111)-like facet in the latter case, as no minimum was found at the facet central hollow site. Due to this distinct behaviour these particular cases are not further considered in the following discussion, avoiding conformational aspects.

In general terms comparable low E_{ads} are found for cuboctahedral Pt₄₄@Cu₉₆ octahedral Pt₄₄@Cu₁₀₂ NPs of -143 and -155 kJ·mol⁻¹, possibly implying a destabilization due to the electron density of the underlying Pt atom, being NO adsorbed on an *hcp* hollow on particularly compact NPs, a factor that would soften anyway with size, though. For the Cu@Pt nanoparticles the E_{ads} range from -94 kJ·mol⁻¹ for octahedral Cu₄₄@Pt₁₀₂ to -204 kJ·mol⁻¹ for icosahedral Cu₅₅@Pt₉₂. Again, the very low adsorption energies for Cu₄₄@Pt₉₆ and Cu₄₄@Pt₁₀₂ are attributed to the repelling subsurface density of the underlying Cu atoms in such compact NPs. Finally the adsorption energy of the rather large cuboctahedral Cu₈₅@Pt₁₄₀ NP of -98 kJ·mol⁻¹ is also very low, but here the origin is different, as Cu₈₅@Pt₁₄₀

belongs to a slightly distorted geometry where NO attaches on a bridge position, similar to the above-commented cases.

Comparing the two bimetallic core@shell systems, the general trend is that the adsorption of NO is stronger on Pt@Cu particles than on Cu@Pt systems by, at least, ~ 17 $\text{kJ}\cdot\text{mol}^{-1}$. This amounts to NO being weaker bound on Cu@Pt NPs, and thus, being more prompt to react, as experimentally observed for NO reduction on Cu@Pt NPs.^[14] Note that for that conclusion only regular octahedral and cuboctahedral system sites were considered, while *e.g.* bridge sites were found for icosahedral and spherical Pt@Cu NPs, as above commented. Notice as well that the high E_{ads} for Cu₄₃@Pt₉₂ of -281 $\text{kJ}\cdot\text{mol}^{-1}$ responds to a severe deformation of the unsaturated surface Pt metal atoms on the surface upon NO adsorption, creating an isolated surface Pt₅ island, whose low CN is responsible of the high computed E_{ads} ; however, this specific singularity is not regarded for the general trend analysis.

Aside from coordination effects, the negative charge of shell Pt atoms, as observed in Figure 5, is detrimental to the NO molecule attachment through its $N^{\delta-}$ atom; moreover, the depletion of the d_z^2 bonds formerly oriented towards the NP vacuum inhibit as well the bonding of the NO molecule. Besides, one can have a look to the electronic structure, considering the ϵ_d effect of bimetallic core@shell NPs, one could regard the d -band centre of the full NP or split into the core and shell phases. Table 7 contains the ϵ_d values for such shell phases, enabling to detect that, in the case of Pt@Cu NPs, the values range from -1.87 to -2.03 eV, where, naturally, the highest values belongs to the smallest NPs, and in all cases is higher than the aforementioned bulk Cu and Cu (111) limit cases. This rise of ϵ_d goes along with the above-commented loss of electrons. On the contrary, for Cu@Pt NPs, the ϵ_d values range from -2.21 to -2.64 eV, displaying the same size dependence as for the Pt@Cu NPs. Again, this lowering in ϵ_d is consistent with the charge transferred to the Pt phase. Such significantly lower energy values of ϵ_d for Cu@Pt NPs are in quite good agreement with the smaller E_{ads} of NO, being, in mean terms, 17 $\text{kJ}\cdot\text{mol}^{-1}$ smaller than the Pt@Cu counterparts, see Table 6. This evaluation further supports the bimetallic core@shell effect on NO attachment when dealing with CuPt NPs. NO would naturally attach stronger to Pt_{*n*} than to Cu_{*n*} NPs, but the bimetallic core@shell structuring implies a charge transfer and a levelling of the electron density, which makes the Pt shell in Cu@Pt less active, ultimately biasing the adsorption strength. The fine detail is thus the remaining electronic levels after the charge transfer, which makes the exposed Pt atoms even less active than Cu shell atoms would be,

making thus the Cu@Pt NPs systems ideal catalysts according to *Le Sabatier* principle, as they only moderately strongly attach NO, enough though to prompt its easier reduction.

As for the monometallic Pt_n and Cu_n NPs, the charge transfer that goes along with the adsorption of NO has been studied for the bimetallic Pt@Cu and Cu@Pt NPs. The Bader charges analysis reveals an electron movement to the adsorbed NO molecule, and the amount of it is listed in Table 7. There, the only remarkable aspect is that on Pt@Cu NPs, a charge transfer of $\sim 0.6 e$ is found, being very similar to the observed cases in Cu_n NPs, see Table 5. Accordingly, a charge transfer of about $\sim 0.5 e$ is found for Cu@Pt NPs. All these values, alongside with the similar NO bond elongations, see Table 6, suggest a similar bonding mechanism.

Moreover, the CDD analyses carried out on the Pt₄₄@Cu₉₆ and Cu₄₄@Pt₉₆, see Figure 7, further supports that picture. The CDD of the Cu₄₄@Pt₉₆ case shows that NO is attached to a slightly positively charged surface region, while negative charge is accumulating around the N atom and near the surface Pt atoms, with no direct participation of the Cu atom underneath. As observed for the Pt₁₄₀ NP CDD, see Figure 6, the NO molecule experiences electron depletion from the 2σ orbital and there is electron accumulation in d_{xz} and d_{yz} character Pt orbitals of the surface Pt atoms, as well as in the aforementioned $2\pi^*$ orbital of NO. Actually, the Cu₄₄@Pt₉₆ picture is consistent with the donation/backdonation bonding mechanism of Pt₁₄₀, but without the role of the subsurface Pt atom. Analogously, the CDD of Pt₄₄@Cu₉₆ reveals the same features as the Cu₁₄₀ did, but here, with a charge accumulation on the d_z^2 orbitals of the underlying Pt atom. In a very simple look, the Cu@Pt or Pt@Cu NP systems retain the bonding chemical activity of the shell metal, but with the electronic modulation of the core metal.

3. Conclusions

Monometallic Pt and Cu nanoparticles, as well as bimetallic core@shell Pt@Cu and Cu@Pt NPs have been investigated regarding their geometries, their electronic properties, and their behaviour upon NO adsorption. For all particles octahedral, cuboctahedral, icosahedral, and spherical-like structures have been modelled in various sizes ranging from 13 to 309 atoms. For monometallic Pt_n and Cu_n NPs the cohesive energies per atom and the mean metal-metal distances linearly evolve with the NP size. Octahedral and icosahedral shapes are preferred for NP diameters below $\varnothing \sim 1.9$ and 1.7 nm for Pt_n and Cu_n, respectively. Above these

dimensions, Wulff-shaped cuboctahedral NPs are energetically preferred, and should be used as models for larger NPs.

As far as bimetallic core@shell Pt@Cu and Cu@Pt NPs are considered, their excess energies reveal that Cu@Pt nanoparticles are more stable, specially cuboctahedral; the Pt@Cu NPs instability decreases with size. These findings explain the experimental stability of Cu@Pt NPs, and that Pt@Cu NPs convert into a CuPt alloy under working conditions, in terms of thermodynamic stability, instead of the proposed Kinkendall effect.^[14] A charge transfer analysis reveals Cu and Pt charges of ~ 0.1 and $-0.1 e$ for Pt@Cu and Cu@Pt NPs, respectively, where on Pt@Cu the charge is invested in the core/shell cohesion, whereas on Cu@Pt it seems that the d_z^2 Pt orbitals oriented towards the vacuum reorganize along the shell. The resulting negative charge of such Pt atoms on Cu@Pt NPs goes along with the reduced NO adsorption strength.

When NO is adsorbed on the studied systems, its attachment over three-fold hollow sites in the middle of (111) or (111)-like facets exhibits, in general terms, a higher adsorption energy on Pt_n NPs, by $\sim 14 \text{ kJ}\cdot\text{mol}^{-1}$, compared to Cu_n. Particularly biasing on the adsorption strength are the presence of a metal atom of the subsurface layer in *hcp* sites, or the low coordination of the second neighbouring surface metal sites, specially when located at NP edge sites. A CDD analysis discloses a donation/back-donation mechanism, which slightly weakens the NO bond, and where subsurface Pt atom on an *hcp* site participates.

On the bimetallic core@shell Pt@Cu and Cu@Pt NPs, the E_{ads} values on Pt@Cu systems are comparable to Cu_n. For Cu@Pt smaller energies are found, in general, by $\sim 17 \text{ kJ}\cdot\text{mol}^{-1}$. This weaker NO adsorption goes along with the experimental results, where an enhanced activity is found for bimetallic Cu@Pt nanoparticles.^[14] The amount of charge transfer towards NO is found to be similar in both types of core@shell NPs, and the CDD plots simply show a mixture of features of the CDD plots of the monometallic NPs, where, apparently, it is the reorganization of the electronic states that makes the shell Pt atoms much less active, a factor that can be similarly relevant for other species, as, *e.g.*, SO_x species known to act as a poison in NSR catalysts.

4. Computational Details

4.1. Simulations

All present DFT calculations were performed using the Vienna *Ab initio* Simulation Package (*VASP*).^[32] Valence electrons were described *via* Kohn-Sham (*KS*) single-electron wave functions and expanded in a plane wave basis with an optimized energy cutoff of 415 eV. Core electrons were described within the Projector Augmented Wave (*PAW*) framework. The exchange correlation contribution to the DFT energy and the *KS* potential were treated through the Perdew-Burke-Ernzerhof (*PBE*) functional,^[33] an exchange-correlation functional within the Generalized Gradient Approximation (*GGA*) found to be the best compromise in describing transition metal bulk and surface properties.^[34] Previous studies did not reveal any noticeable spin-polarization effect for the substrate models or the adsorption complexes of NO molecules on them.^[27] Thus, all calculations were carried out in a non spin-polarized fashion way, except for the ones of the free NO molecule and single Cu or Pt atoms, for which spin-polarized calculations in an asymmetric cell of $9 \times 10 \times 11$ Å were carried out to achieve correct orbital occupancies.

The structure of all NPs, adsorbates, and surfaces were optimized such that the forces on all relaxed atoms were less than 0.03 eV/Å with an energetic convergence criterion of 10^{-5} eV for self-consistent cycles. The NPs were placed in a unit cell with at least 3.5 Å vacuum on all sides such that periodic images were separated by at least 7 Å. The Brillouin zone was sampled at the Γ -point, and the second order method of Methfessel-Paxton^[35] with a smearing width of 0.1 eV was used for determining partial occupancies of states near the Fermi level, although final total energies were extrapolated to zero smearing. Slab calculations were performed using a $p(3 \times 3)$ supercell with six layers to simulate the (111) surfaces, with the bottom three layers held frozen in PBE bulk-optimized positions, and adding 10 Å of vacuum to avoid interaction in between slabs.^[34,36] The Brillouin zone of the slabs were sampled using a $9 \times 9 \times 1$ Monkhorst-Pack^[37] k -point mesh, also integrated using the method of Methfessel-Paxton with a smearing width of 0.1 eV.

In order to compare the NO adsorption results in between the Pt and Cu (111) slab models, and the modelled NPs, the adsorption was only regarded on the (111) facets of octahedral, cuboctahedral, and spherical-like NPs. The icosahedral particles are an exception, because they do not display (111) facets because of the different bulk arrangement. Still, the triangular structure of their facets is comparable to some extent to pure (111) facets, being

(111)-like, and have been examined accordingly. It is known that NO adsorbs in *fcc* hollow positions on both Cu and Pt (111) surfaces,^[38,39] and consequently, this site has been the target in the adsorption of NO on the modelled (111) slab models and monometallic and core@shell NPs. In the NPs models the site sampled was that in the centre of (111) or (111)-like facets. However, in some NPs, that belonged to an hexagonal close-packed (*hcp*) hollow site, or to a top site. Therefore NO has been adsorbed as much centred as possible, which sometimes resulted in the adsorption on a *hcp* hollow site, whose reference on Cu and Pt (111) slabs has been gained as well, with the ultimate goal of shedding light on the core@shell effects on NO adsorption, and by restricting the adsorptive landscape reducing/neglecting low-coordination effects, focusing thus only on size, shape, and compositions effects. The adsorption energy, E_{ads} , has been defined as

$$E_{ads} = E_{NO/NP} - E_{NO} - E_{NP} \quad (1),$$

where E_{NO} is the energy of the isolated NO molecule, E_{NP} the energy of isolated, pristine employed NP —either monometallic or core@shell bimetallic, and $E_{NO/NP}$ the energy of the employed NP having NO adsorbed upon. With this definition, the more negative the E_{ads} is, the stronger the adsorption of NO upon.

4.2. Nanoparticle Models

Monometallic Pt and Cu NPs of various shapes and sizes as well as bimetallic Cu@Pt and Pt@Cu NPs have been modelled prior to NO adsorption upon. These monometallic NPs are denoted Pt_n or Cu_n , where n is the number of atoms in the NP. Bimetallic NPs use the core@shell notation, so a Cu@Pt NP has a Cu core and a Pt shell. Here again a subscript describes the number of atoms of the element, *e.g.* a $Cu_{44}@Pt_{96}$ NP has 44 core atoms of Cu and 96 Pt shell atoms, which makes in total 140 atoms in the nanoparticle.

Different monometallic NPs shapes have been considered maintaining the *fcc* crystallographic structure. To this end octahedral, cuboctahedral, and spherical-like shapes have been considered. The octahedral models comprise sizes of $n = 19, 44, 85, 146,$ and 231 displaying only (111) facets, see Figure 8. The cuboctahedral models encompass sizes of $n = 13, 38, 79, 140,$ and 225 atoms, displaying small (001) facets in addition to the (111) ones, see Figure 8. Notice that such shapes are those belonging to Wulff constructions minimizing the overall monometallic NP surface tension.^[40] Further capping of (001) surfaces shapes have been acquired from $n = 140$ and 225 cuboctahedra, creating nanoparticles with larger (001) facets and $n = 116$ or 201 , see Figure 8.

Structures with spherical-like shapes have been modelled from bulk supercells defining a NP diameter, \varnothing , so that all atoms exceeding such diameter were removed. In that way particles of $n = 13, 43, 62, 135,$ and 260 were achieved, see Figure 9. One can clearly observe that such NPs do not have a real spherical shape, but rather a slightly higher concentration of steps and surface defects, but nevertheless are still categorized as *spherical* like. The last class of geometries, icosahedra, are also displayed in Figure 9, with $n = 13, 55, 147,$ and 309 , even though the crystallographic structure is not *fcc* anymore. The Pt and Cu NPs have been initially built up using the bulk PBE cell parameters,^[36] but afterwards have been fully optimized. As a note of caution, the cuboctahedral and spherical $n = 13$ clusters are actually the same geometrical structure.

Bimetallic Pt@Cu and Cu@Pt NP models were built from optimized monometallic Cu and Pt NPs particles, replacing the outermost shell by the other metal, *e.g.* the Cu₄₄@Pt₉₆ particle has been gained from Cu₁₄₀, replacing the 96 Cu atoms of the outer shell by Pt and fully optimizing the resulting structure. Note that for cuboctahedral Cu₃₈@Pt₇₈ and Cu₇₉@Pt₁₂₂ NPs the core is cuboctahedral, whereas for cuboctahedral Cu₄₄@Pt₉₆ and Cu₈₅@Pt₁₄₀ NPs as well as for octahedral Cu₄₄@Pt₁₀₂ and Cu₈₅@Pt₁₄₆ NPs the core is octahedral. From the construction procedure all icosahedral core@shell structures have an icosahedral core. Finally, the spherical-like Cu₄₃@Pt₉₂ particle has a spherical-like core. On the contrary, the Cu₁₁₆@Pt₁₄₄ case has a cuboctahedral core. All core@shell NP geometries of the Cu@Pt type are displayed in Figure 10. Note that only relatively large bimetallic core@shell systems have been modelled. The reason is that cores with a metallic electronic character should be considered, aiming at using these models to describe much larger NPs and thus being in the scalable regime, as shown in the past for late transition metal NPs.^[22,23] Note that experimentally investigated core@shell NPs have \varnothing between ~ 9 and ~ 18 nm for Cu@Pt and Pt@Cu, respectively.^[14]

Acknowledgements

The authors gratefully acknowledge the funding of the German Research Council (DFG), which, within the framework of its “Excellence Initiative”, supports the Cluster of Excellence “Engineering of Advanced Materials” (www.eam.uni-erlangen.de) at the University of Erlangen-Nuremberg. F.V. thanks the Alexander von Humboldt Foundation for his postdoctoral grant, and the *Ministerio de Economía y Competitividad* (MEC) for his

Ramón y Cajal (RYC-2012-10129) research contract. Both A.G. and F.V. are thankful to MSc. Nicola Luckas for her kind help and for fruitful discussions during the early stages of the study. The research carried out at the *Universitat de Barcelona* has been supported by the Spanish MICIUN/FEDER RTI2018-095460-B-I00 and *María de Maeztu* MDM-2017-0767 grants and, in part, by *Generalitat de Catalunya* 2017SGR13 and XRQTC grants.

Figure 1. Cohesive energy E_{coh} and average metal-metal distance $d(M-M)$ of Cu_n (blue) and Pt_n (green) NPs as function of the NP size defined as $n^{-1/3}$ with n denoting the number of atoms of the NP.

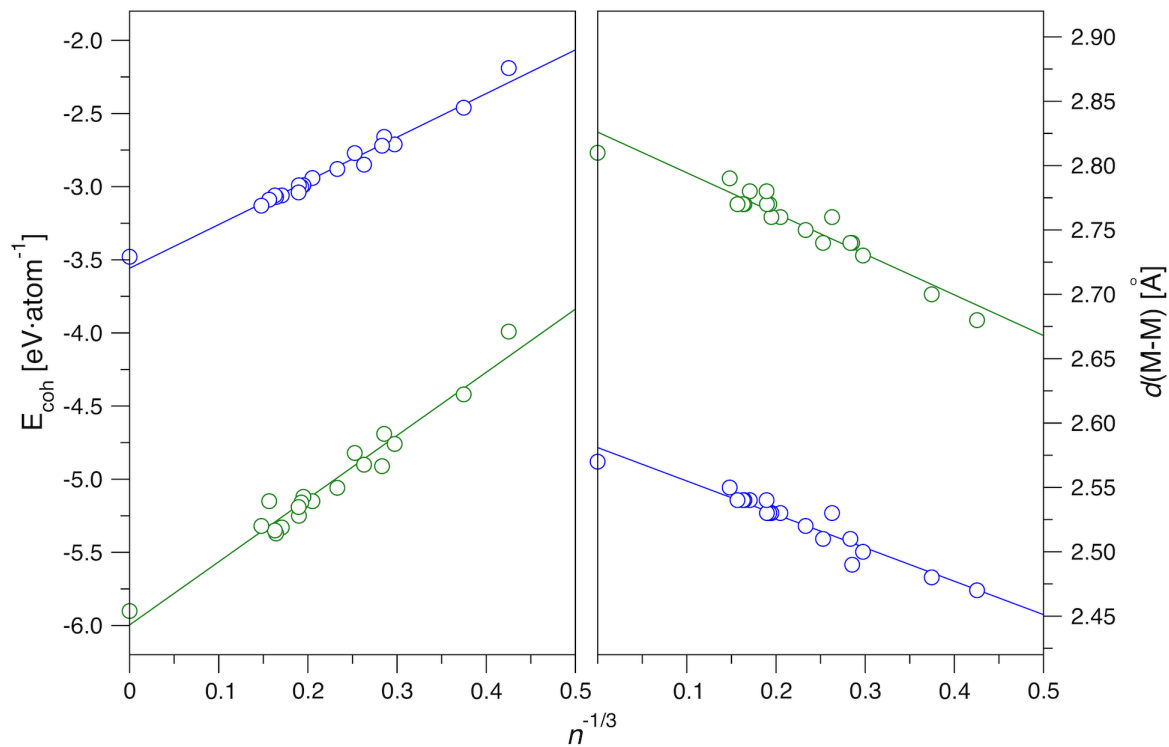


Figure 2. Cohesive energy E_{coh} of Cu_n (left panel) and Pt_n (right panel) clusters and NPs with different shapes, including octahedral (turquoise), cuboctahedral (black), spherical-like (orange), and icosahedral (red) ones, displaying calculated points (circles), and the adjusted linear regression trend (solid lines). The cohesive energy E_{coh} is given as function of the NP size defined as $n^{-1/3}$ with n denoting the number of atoms of the NP.

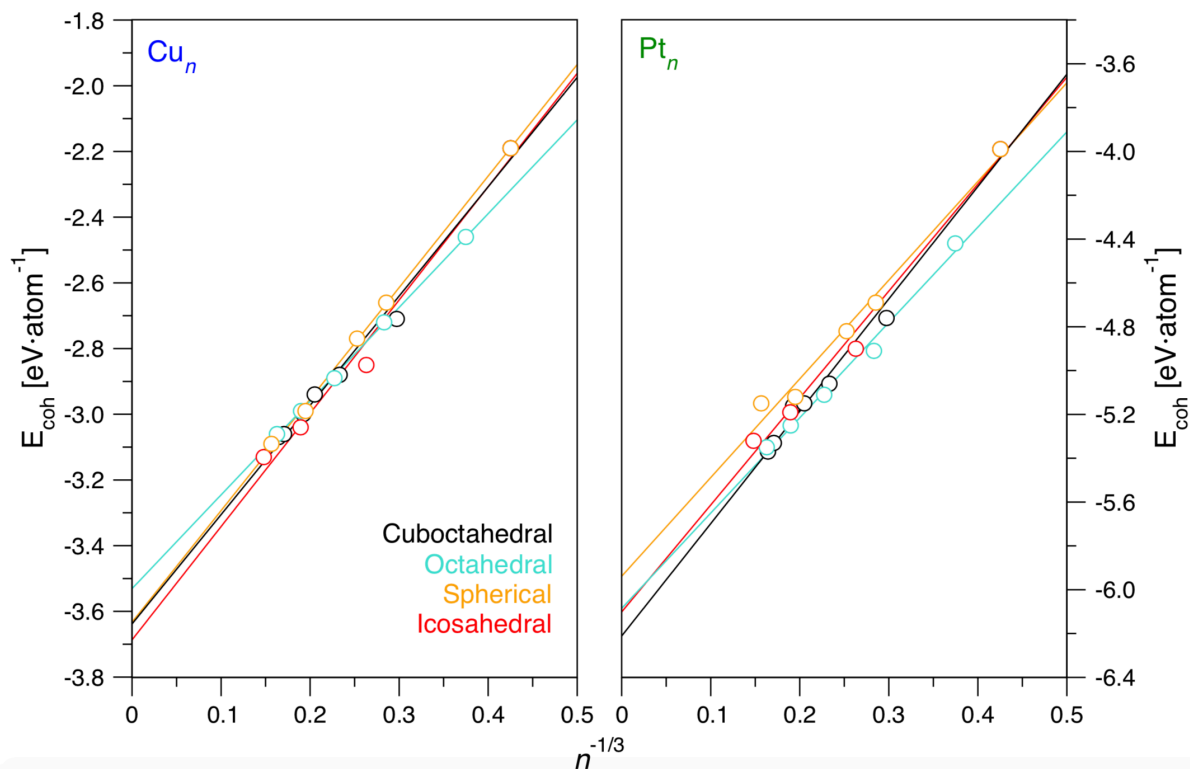


Figure 3. Cohesive energy E_{coh} of $Pt_j@Cu_i$ (open circles) and $Cu_i@Pt_j$ (filled circles) NPs with different shapes, including octahedral (turquoise), cuboctahedral (black), spherical-like (orange), and icosahedral (red) ones. The cohesive energy E_{coh} is given as function of the NP size defined as $n^{-1/3}$ with n denoting the number of atoms of the NP.

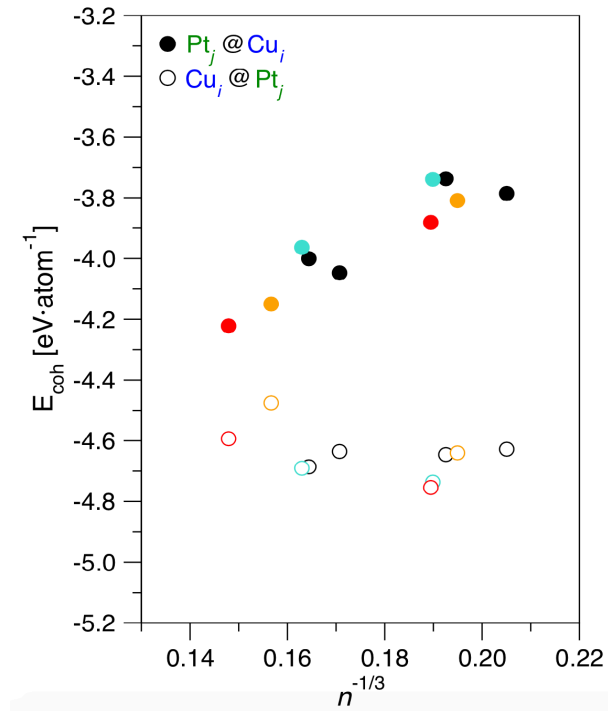


Figure 4. Charge per atom Q for Pt@Cu (open circles) and Cu@Pt (filled circles) NPs in units of the elementary charge of the electron e .

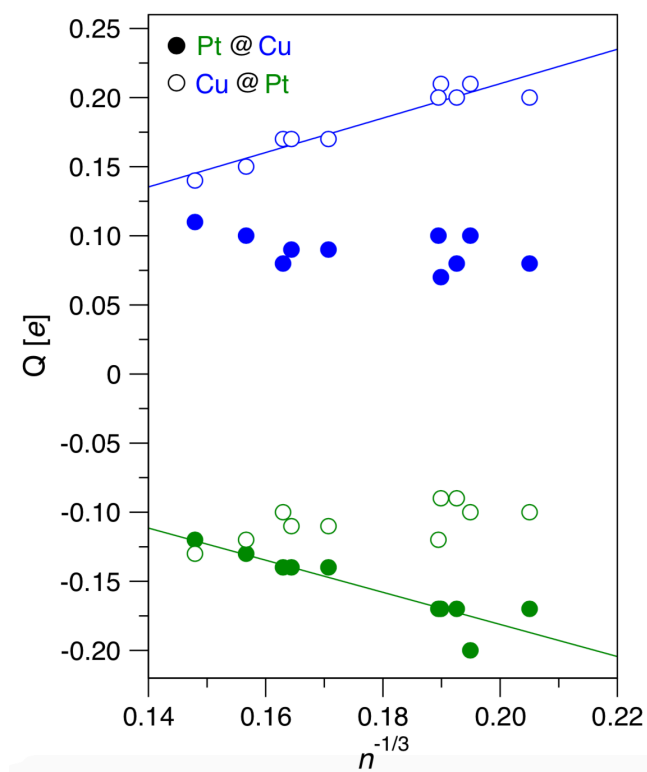


Figure 5. Charge density difference (*CDD*) plots for Pt₄₄@Cu₉₆ (left) and Cu₄₄@Pt₉₆ (right). Green and blue spheres denote Pt and Cu atoms, respectively. Blue globes denote charge depletion while mauve globes indicate charge accumulation. An isovalue of ± 0.04 a.u. is used in the CDD contours.

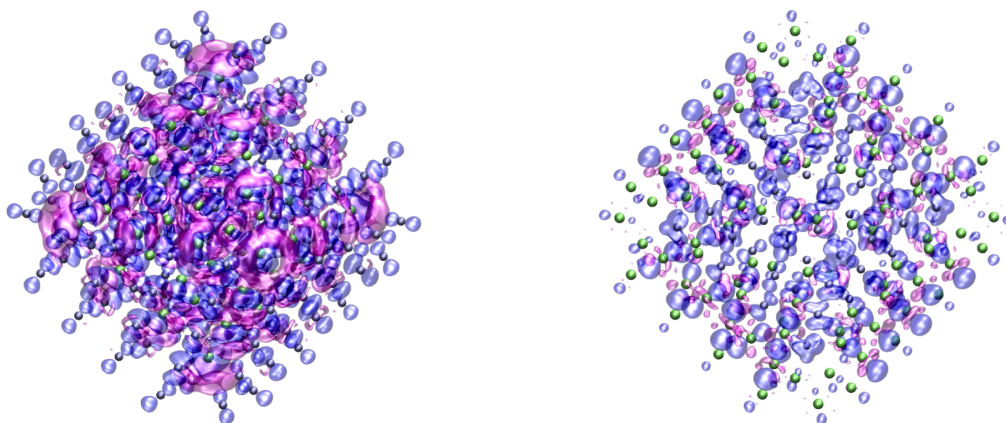


Figure 6. Charge density difference (*CDD*) plots for NO adsorbed on Pt₁₄₀ (left) and Cu₁₄₀ (right). Green, blue, turquoise, and red spheres denote Pt, Cu, N, and O atoms, respectively. Blue globes denote charge depletion while mauve globes indicate charge accumulation. An isovalue of ± 0.04 a.u. was used for the CDD contours.

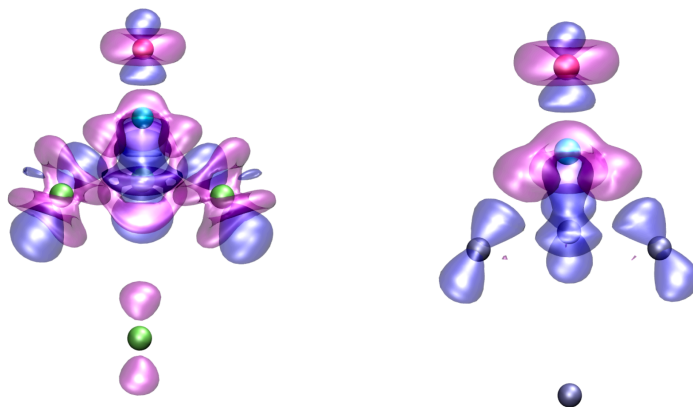


Figure 7. Charge density difference (*CDD*) plots for NO adsorbed on Pt₄₄@Cu₉₆ (left) and Cu₄₄@Pt₉₆ (right). Green, blue, turquoise, and red spheres denote Pt, Cu, N, and O atoms, respectively. Blue globes denote charge depletion while mauve globes indicate charge accumulation. An isovalue of ± 0.04 a.u. was used for the *CDD* contours.

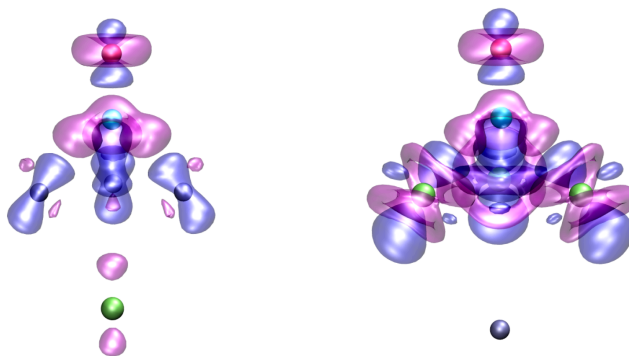


Figure 8. Octahedral (top row) and cuboctahedral (middle and bottom rows) monometallic Pt_n NPs. Green spheres denote Pt atoms.

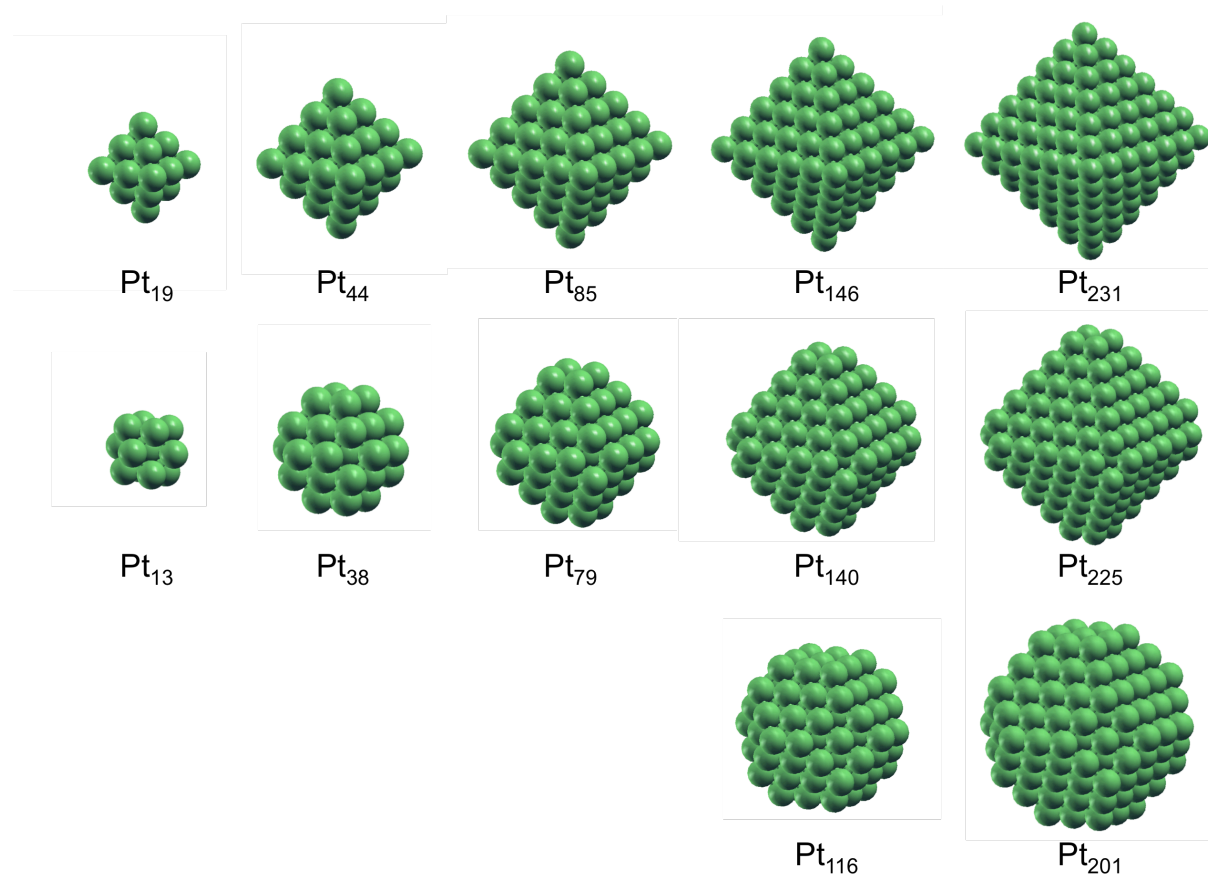


Figure 9. Spherical-like (top row) and icosahedral (bottom row) monometallic Pt_n NPs.

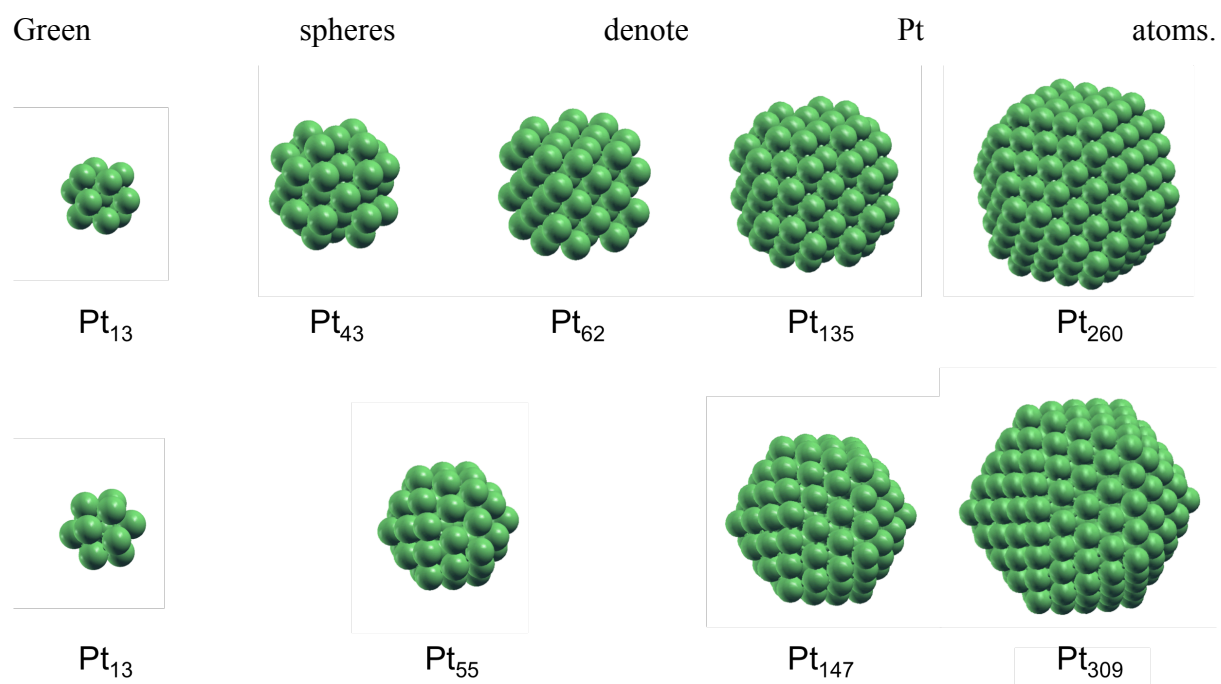


Figure 10. Bimetallic core@shell Cu@Pt NPs. Cu and Pt atoms are denoted by blue and green spheres, respectively. The atomic radii have been reduced to enable a visualization of the underlying Cu core.

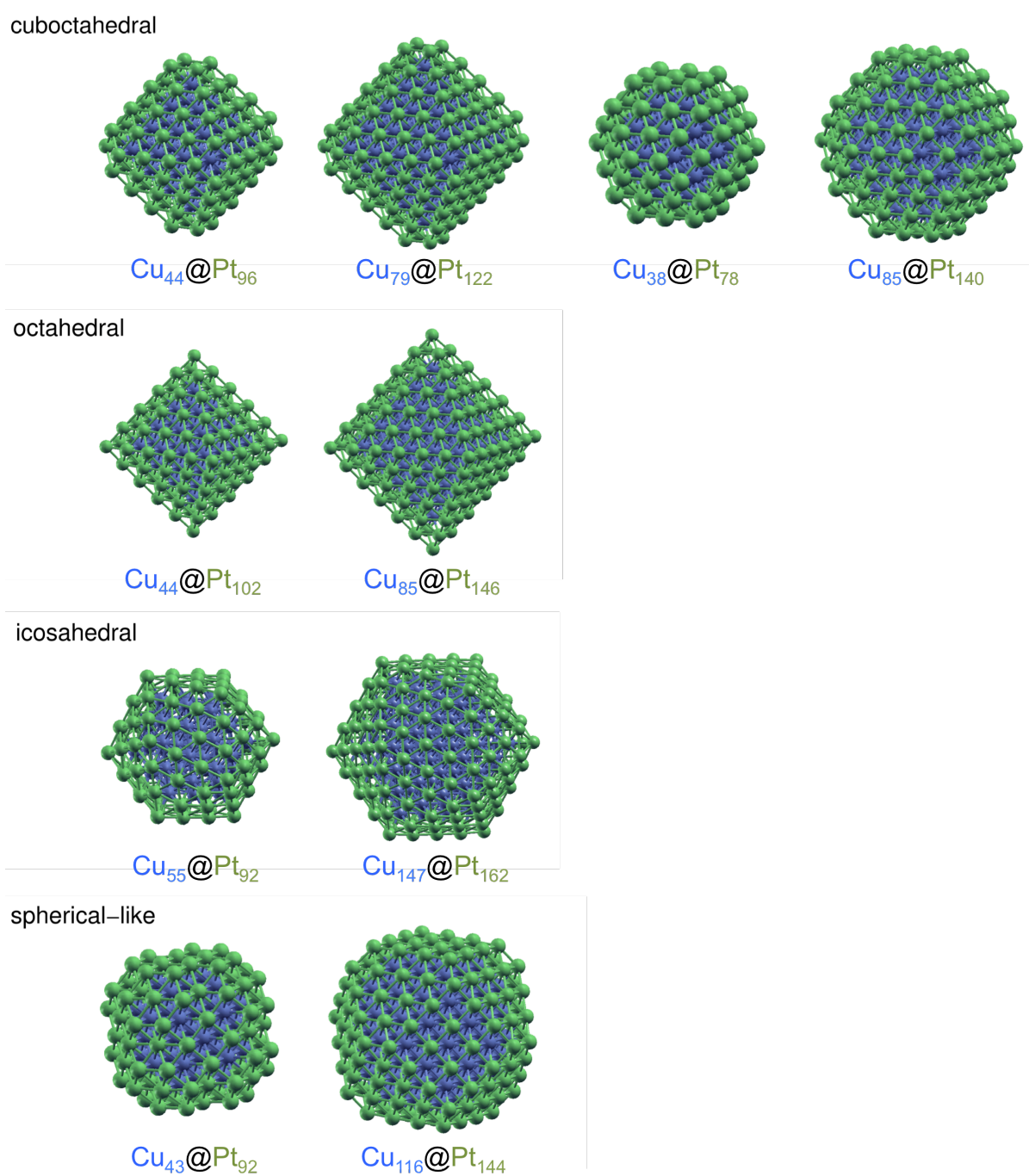


Table 1. Slopes (a) and intercepts (b) of the regression coefficients of cohesive energies E_{coh} with respect to $n^{-1/3}$, according to $E_{coh} = a \cdot n^{-1/3} + b$, corresponding to the shape analysis shown in Figure 2. The number of atoms is denoted by n . The linear adjustment regression coefficient values R are also shown.

	Cu_n			Pt_n		
	<i>a</i>	<i>b</i>	<i>R</i>	<i>a</i>	<i>b</i>	<i>R</i>
Octahedral	2.85	-3.53	0.9998	4.35	-6.08	0.9925
Cuboctahedral	3.33	-3.64	0.9948	5.13	-6.21	0.9952
Icosahedral	3.45	-3.69	0.9925	4.88	-6.10	0.9946
Spherical	3.39	-3.63	0.9995	4.50	-5.94	0.9925

Table 2. Excess energy E_{exc} and average Pt-Pt, Cu-Cu, and Pt-Cu nearest neighbor distances, $d(\text{Pt-Pt})$, $d(\text{Cu-Cu})$, and $d(\text{Cu-Pt})$, respectively, of the investigated Pt@Cu and Cu@Pt bimetallic NPs. E_{exc} values are given in meV, whereas the average distances, d , are given in Å.

Shape	Size	E_{exc}	$d(\text{Pt-Pt})$	$d(\text{Cu-Cu})$	$d(\text{Cu-Pt})$
Octahedral	Pt ₄₄ @Cu ₁₀₂	-68	2.80	2.59	2.63
	Pt ₈₅ @Cu ₁₄₆	-61	2.80	2.62	2.63
Cuboctahedral	Pt ₃₈ @Cu ₇₈	-122	2.79	2.64	2.60
	Pt ₄₄ @Cu ₉₆	-69	2.78	2.63	2.62
	Pt ₇₉ @Cu ₁₂₂	-95	2.79	2.64	2.61
	Pt ₈₅ @Cu ₁₄₀	-62	2.79	2.64	2.63
Icosahedral	Pt ₅₅ @Cu ₉₂	-37	2.80	2.76	2.56
	Pt ₁₄₇ @Cu ₁₆₂	-50	2.80	2.75	2.59
Spherical	Pt ₄₃ @Cu ₉₂	-141	2.80	2.61	2.63
	Pt ₁₁₆ @Cu ₁₄₄	-141	2.80	2.67	2.61
Octahedral	Cu ₄₄ @Pt ₁₀₂	-168	2.66	2.60	2.74
	Cu ₈₅ @Pt ₁₄₆	-183	2.67	2.60	2.73
Cuboctahedral	Cu ₃₈ @Pt ₇₈	-202	2.66	2.56	2.72
	Cu ₄₄ @Pt ₉₆	-165	2.66	2.60	2.74
	Cu ₇₉ @Pt ₁₂₂	-198	2.66	2.59	2.72
	Cu ₈₅ @Pt ₁₄₀	-185	2.66	2.60	2.73
Icosahedral	Cu ₅₅ @Pt ₉₂	-286	2.69	2.58	2.70
	Cu ₁₄₇ @Pt ₁₆₂	-299	2.68	2.59	2.71
Spherical	Cu ₄₃ @Pt ₉₂	-79	2.67	2.59	2.69
	Cu ₁₁₆ @Pt ₁₄₄	-209	2.66	2.58	2.70

Table 3. Overall charges Q_{Pt} and Q_{Cu} of the Pt and Cu phases, respectively, as well as the charge per atom $Q_{\text{Pt}}^{\text{at}}$ and $Q_{\text{Cu}}^{\text{at}}$, respectively. All values are given in units of the elementary charge e of the electron.

Shape	Size	Q_{Pt}	Q_{Cu}	$Q_{\text{Pt}}^{\text{at}}$	$Q_{\text{Cu}}^{\text{at}}$
Octahedral	Pt ₄₄ @Cu ₁₀₂	-7.17	7.17	-0.17	0.07
	Pt ₈₅ @Cu ₁₄₆	-11.59	11.59	-0.14	0.08
Cuboctahedral	Pt ₃₈ @Cu ₇₈	-6.36	6.36	-0.17	0.08
	Pt ₄₄ @Cu ₉₆	-7.32	7.32	-0.17	0.08
	Pt ₇₉ @Cu ₁₂₂	-11.20	11.20	-0.14	0.09
	Pt ₈₅ @Cu ₁₄₀	-11.90	11.90	-0.14	0.09
Icosahedral	Pt ₅₅ @Cu ₉₂	-9.45	9.45	-0.17	0.10
	Pt ₁₄₇ @Cu ₁₆₂	-18.15	18.15	-0.12	0.11
Spherical	Pt ₄₃ @Cu ₉₂	-8.60	8.60	-0.20	0.10
	Pt ₁₁₆ @Cu ₁₄₄	-15.04	15.04	-0.13	0.10
Octahedral	Cu ₄₄ @Pt ₁₀₂	9.19	-9.19	-0.09	0.21
	Cu ₈₅ @Pt ₁₄₆	14.66	-14.66	-0.10	0.17
Cuboctahedral	Cu ₃₈ @Pt ₇₈	7.50	-7.50	-0.10	0.20
	Cu ₄₄ @Pt ₉₆	8.99	-8.99	-0.09	0.20
	Cu ₇₉ @Pt ₁₂₂	13.03	-13.03	-0.11	0.17
	Cu ₈₅ @Pt ₁₄₀	14.77	-14.77	-0.11	0.17
Icosahedral	Cu ₅₅ @Pt ₉₂	10.76	-10.76	-0.12	0.20
	Cu ₁₄₇ @Pt ₁₆₂	20.56	-20.56	-0.13	0.14
Spherical	Cu ₄₃ @Pt ₉₂	9.00	-9.00	-0.10	0.21
	Cu ₁₁₆ @Pt ₁₄₄	17.06	-17.06	-0.12	0.15

Table 4. Computed adsorption energies E_{ads} in $\text{kJ}\cdot\text{mol}^{-1}$ of the central three-fold hollow sites on the investigated Pt_n and Cu_n NPs (111) or (111)-like facets, for the different sizes n and shapes, as well as for Pt and Cu (111) surface slab models. For each site, the hollow site is tagged as *fcc* and *hcp* when possible. For each found minimum, the NO molecular distance $d(\text{N-O})$, the height h of the N atom to the (111) facet or surface, the mean distance $d(\text{N-Pt})$ and $d(\text{N-Cu})$ of N to the Pt or Cu surface hollow atoms, respectively, and the mean distances $d(\text{Pt-Pt})$ and $d(\text{Cu-Cu})$ between such surface hollow Pt and Cu atoms are shown. All distances given in Å.

Metal	Shape	n	site	E_{ads}	$d(\text{N-O})$	h	$d(\text{N-Pt})$	$d(\text{Pt-Pt})$	$d(\text{N-Cu})$	$d(\text{Cu-Cu})$
Pt	Octahedral	146	<i>hcp</i>	-164	1.21	1.30	2.08	2.82	—	—
		231	<i>fcc</i>	-183	1.21	1.28	2.07	2.81	—	—
	Cuboctahedral	116	<i>hcp</i>	-192	1.21	1.25	2.06	2.83	—	—
		140	<i>hcp</i>	-170	1.21	1.28	2.07	2.81	—	—
		201	<i>fcc</i>	-197	1.22	1.24	2.06	2.84	—	—
	Icosahedral	225	<i>fcc</i>	-187	1.21	1.26	2.06	2.83	—	—
		147	—	-203	1.22	1.13	2.09	3.04	—	—
		309	—	-225	1.22	1.17	2.06	2.94	—	—
	Spherical	135	<i>fcc</i>	-204	1.22	1.32	2.09	2.80	—	—
		260	<i>fcc</i>	-193	1.22	1.23	2.05	2.86	—	—
	(111) Slab	<i>fcc</i>		-198	1.21	1.22	2.09	2.93	—	—
		<i>hcp</i>		-184	1.21	1.26	2.09	2.88	—	—
Cu	Octahedral	146	<i>hcp</i>	-173	1.22	1.28	—	—	1.99	2.63
		231	<i>fcc</i>	-191	1.22	1.32	—	—	2.00	2.60
	Cuboctahedral	116	<i>hcp</i>	-155	1.23	1.27	—	—	1.99	2.65
		140	<i>hcp</i>	-141	1.22	1.33	—	—	2.01	2.61
		201	<i>fcc</i>	-179	1.23	1.32	—	—	2.00	2.60
	Icosahedral	225	<i>fcc</i>	-185	1.22	1.30	—	—	1.99	2.63
		147	—	-166	1.23	1.32	—	—	2.02	2.67
		309	—	-247	1.23	1.25	—	—	2.00	2.72
	Spherical	135	<i>fcc</i>	-184	1.23	1.27	—	—	2.03	2.69
		260	<i>fcc</i>	-226	1.22	1.28	—	—	1.99	2.64
	(111) Slab	<i>fcc</i>		-143	1.22	1.28	—	—	2.00	2.65
		<i>hcp</i>		-140	1.22	1.28	—	—	2.00	2.65

Table 5. Bader charges Q_{Pt} and Q_{Cu} of Pt and Cu NPs, respectively, as well as the Bader charges Q_{NO} of the adsorbed NO. All values given in units of the elementary charge e of the electron. Reference values for the Pt and Cu (111) slab are also given.

Shape	Pt		Cu			
	n	site	Q_{Pt}	Q_{NO}	Q_{Cu}	Q_{NO}
Octahedral	146	<i>hcp</i>	0.46	-0.46	0.60	-0.60
	231	<i>fcc</i>	0.48	-0.48	0.60	-0.60
Cuboctahedral	116	<i>hcp</i>	0.53	-0.53	0.65	-0.65
	140	<i>hcp</i>	0.47	-0.47	0.61	-0.61
	201	<i>fcc</i>	0.49	-0.49	0.63	-0.63
Icosahedral	225	<i>fcc</i>	0.47	-0.47	0.61	-0.61
	147	—	0.53	-0.53	0.65	-0.65
	309	—	0.50	-0.50	0.64	-0.64
Spherical	135	<i>fcc</i>	0.51	-0.51	0.60	-0.60
	260	<i>fcc</i>	0.50	-0.50	0.61	-0.61
(111) Slab		<i>fcc</i>	0.70	-0.70	0.64	-0.64
		<i>hcp</i>	0.71	-0.71	0.64	-0.64

Table 6. Adsorption energy E_{ads} of NO on threefold hollow sites at the center of (111)-facets of Pt@Cu and Cu@Pt NPs. For any given adsorption structure the distance, d , between N and O atoms of the molecules, $d(\text{N-O})$, are given as well as the height h of the N atom to the (111) facet. Finally, direct distances of N to the surface Pt or Cu atoms, $d(\text{N-Pt})$ and $d(\text{N-Cu})$, respectively, and the Pt-Pt and Cu-Cu distances $d(\text{Pt-Pt})$ and $d(\text{Cu-Cu})$ of the directly binding Pt or Cu atoms are listed. Energies are given in $\text{kJ}\cdot\text{mol}^{-1}$ and distances in Å.

Shape	Size	Site	E_{ads}	$d(\text{N-O})$	h	$d(\text{N-Pt})$	$d(\text{Pt-Pt})$	$d(\text{N-Cu})$	$d(\text{Cu-Cu})$
Octahedral	Pt ₄₄ @Cu ₁₀₂	<i>hcp</i>	-143	1.22	1.31	—	—	2.03	2.69
	Pt ₈₅ @Cu ₁₄₆	<i>fcc</i>	-181	1.23	1.25	—	—	2.01	2.73
Cuboctahedral	Pt ₃₈ @Cu ₇₈	<i>hcp</i>	-173	1.23	1.29	—	—	2.02	2.69
	Pt ₄₄ @Cu ₉₆	<i>hcp</i>	-155	1.22	1.30	—	—	2.02	2.69
	Pt ₇₉ @Cu ₁₂₂	<i>fcc</i>	-171	1.23	1.24	—	—	2.01	2.73
Icosahedral	Pt ₈₅ @Cu ₁₄₀	<i>fcc</i>	-169	1.23	1.24	—	—	2.01	2.73
	Pt ₅₅ @Cu ₉₂	—	-162	1.23	1.28	—	—	2.01	2.70
	Pt ₁₄₇ @Cu ₁₆₂	^a	-114	1.21	—	—	—	1.92	3.11
Spherical	Pt ₄₃ @Cu ₉₂	^a	-189	1.21	—	—	—	1.90	2.59
	Pt ₁₁₆ @Cu ₁₄₄	<i>fcc</i>	-181	1.23	1.26	—	—	2.01	2.71
Octahedral	Cu ₄₄ @Pt ₁₀₂	<i>hcp</i>	-94	1.21	1.28	2.05	2.78	—	—
	Cu ₈₅ @Pt ₁₄₆	<i>fcc</i>	-109	1.21	1.29	2.06	2.78	—	—
Cuboctahedral	Cu ₃₈ @Pt ₇₈	<i>hcp</i>	-149	1.22	1.26	2.04	2.79	—	—
	Cu ₄₄ @Pt ₉₆	<i>hcp</i>	-98	1.21	1.27	2.05	2.77	—	—
	Cu ₇₉ @Pt ₁₂₂	<i>fcc</i>	-122	1.22	1.24	2.04	2.82	—	—
Icosahedral	Cu ₈₅ @Pt ₁₄₀	<i>fcc</i>	-98	1.21	1.28	2.06	2.79	—	—
	Cu ₅₅ @Pt ₉₂	—	-204	1.21	1.30	2.08	2.82	—	—
	Cu ₁₄₇ @Pt ₁₆₂	—	-199	1.21	1.24	2.04	2.81	—	—
Spherical	Cu ₄₃ @Pt ₉₂	<i>fcc</i>	-281	1.22	1.29	2.08	2.83	—	—
	Cu ₁₁₆ @Pt ₁₄₄	<i>fcc</i>	-111	1.21	1.31	2.06	2.77	—	—

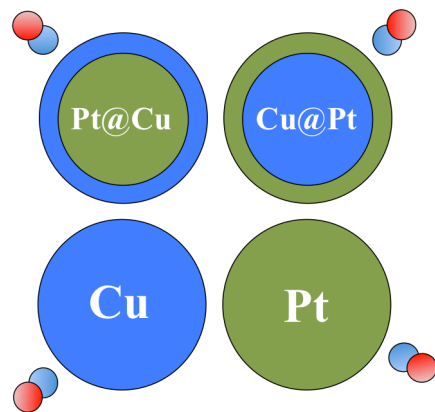
^a bridge site at NP edge.

Table 7. Calculated d -band centers ϵ_d for the studied shell phases of Pt@Cu and Cu@Pt NPs. The d -band centers ϵ_d are given in eV. Charges Q_{NO} of adsorbed NO molecule in units of the elementary charge e of the electron.

Shape	Size	ϵ_d Cu	ϵ_d Pt	Q_{NO}
Octahedral	Pt ₄₄ @Cu ₁₀₂	-2.01	—	-0.59
	Pt ₈₅ @Cu ₁₄₆	-2.02	—	-0.61
Cuboctahedral	Pt ₃₈ @Cu ₇₈	-1.87	—	-0.61
	Pt ₄₄ @Cu ₉₆	-1.99	—	-0.60
	Pt ₇₉ @Cu ₁₂₂	-1.91	—	-0.62
	Pt ₈₅ @Cu ₁₄₀	-2.03	—	-0.61
Icosahedral	Pt ₅₅ @Cu ₉₂	-1.93	—	-0.64
	Pt ₁₄₇ @Cu ₁₆₂	-1.88	—	-0.62
Spherical	Pt ₄₃ @Cu ₉₂	-2.00	—	-0.51
	Pt ₁₁₆ @Cu ₁₄₄	-1.90	—	-0.61
Octahedral	Cu ₄₄ @Pt ₁₀₂	—	-2.53	-0.49
	Cu ₈₅ @Pt ₁₄₆	—	-2.64	-0.46
Cuboctahedral	Cu ₃₈ @Pt ₇₈	—	-2.40	-0.51
	Cu ₄₄ @Pt ₉₆	—	-2.50	-0.52
	Cu ₇₉ @Pt ₁₂₂	—	-2.55	-0.49
	Cu ₈₅ @Pt ₁₄₀	—	-2.61	-0.46
Icosahedral	Cu ₅₅ @Pt ₉₂	—	-2.21	-0.49
	Cu ₁₄₇ @Pt ₁₆₂	—	-2.41	-0.45
Spherical	Cu ₄₃ @Pt ₉₂	—	-2.31	-0.46
	Cu ₁₁₆ @Pt ₁₄₄	—	-2.47	-0.45

Table of Contents

Catalytic activity of core@shell particles: Insights by DFT



References

- [1] N. Toshima, T. Yonezawa, *New J. Chem.* **1998**, *22*, 1179-1201.
- [2] R. Ferrando, J. Jellinek, R. L. Johnston, *Chem. Rev.* **2008**, *108*, 845-910.
- [3] F. Viñes, J. R. B. Gomes, F. Illas, *Chem. Soc. Rev.* **2014**, *43*, 4922-4939.
- [4] F. Calle-Vallejo, J. Tymoczko, V. Colic, Q. H. Vu, M. D. Pohl, K. Morgenstern, D. Loffreda, P. Sautet, W. Schuhmann, A. S. Bandarenka, *Science* **2015**, *350*, 185-189.
- [5] I. V. Yudanov, A. V. Matveev, K. M. Neymann, N. Rösch, *J. Am. Chem. Soc.* **2008**, *130*, 9342-9352.
- [6] F. Viñes, Y. Lykhach, T. Staudt, M. P. A. Lorenz, C. Papp, H.-P. Steinrück, J. Libuda, K. M. Neymann, A. Görling, *Chem. Eur. J.* **2010**, *16*, 6530-6539.
- [7] S. M. Kozlov, G. Kovács, R. Ferrando, K. M. Neyman, *Chem. Sci.* **2015**, *6*, 3868-3880.
- [8] F. Besenbacher, I. Chorkendorff, B. S. Clausen, B. Hammer, A. M. Molenbroek, J. K. Nørskov, I. Stensgaard, *Science* **1998**, *279*, 1913-1915.
- [9] S. Cao, J. Chen, J. Hu. *Aust. J. Chem.* **2009**, *62*, 1561-1576.
- [10] W. Schärfl, *Nanoscale* **2010**, *2*, 829-843.
- [11] N. Toshima, Y. Wang, *Langmuir* **1994**, *10*, 4574-4580.
- [12] C. U. I. Odenbrand, J. Blanco, P. Avila, C. Knapp, *Appl. Catal. B* **1999**, *23*, 37-44.
- [13] J. Libuda, H.-J. Freund, *Surf. Sci. Rep.* **2005**, *57*, 157-298.
- [14] S. Zhou, B. Varughese, B. Eichhorn, G. Jackson, K. McIlwrath, *Angew. Chem. Int. Ed.* **2005**, *44*, 4539-4543.
- [15] Y. D. Din, R. M. Rioux, C. K. Erdonmez, S. Hughes, G. A. Somorjai, A. P. Alivisatos, *Science* **2004**, *304*, 711-714.
- [16] C. Sedlmair, K. Seshan, A. Jentys, J. A. Lercher, *Catal. Today* **2002**, *75*, 413-419.
- [17] I. Nova, L. Lietti, L. Castoldi, E. Tronconi, P. Forzatti, *J. Catal.* **2006**, *239*, 244-254.
- [18] N. Luckas, F. Viñes, M. Happel, A. Desikusumastuti, J. Libuda, A. Görling, *J. Phys. Chem. C* **2010**, *114*, 13813-13824.
- [19] M. Happel, N. Luckas, F. Viñes, M. Sobota, M. Laurin, A. Görling, J. Libuda, *J. Phys. Chem. C* **2011**, *115*, 479-491.
- [20] J. Greeley, M. Mavrikakis, *Nat. Mater.* **2004**, *3*, 810-815.

-
- [21] Z. D. Pozun, K. Tran, A. Shi, R. H. Smith, G. Henkelman, *J. Phys. Chem. C* **2011**, *115*, 1811-1818.
- [22] F. Viñes, F. Illas, K. M. Neyman, *J. Phys. Chem. A* **2008**, *112*, 8911-8915.
- [23] A. Roldán, F. Viñes, F. Illas, J. M. Ricart, K. M. Neyman, *Theor. Chem. Acc.* **2008**, *120*, 565-573.
- [24] T. Rapps, R. Ahlrichs, E. Waldt, M. M. Kappes, D. Schooss, *Angew. Chem. Int. Ed.* **2013**, *52*, 6102-6105.
- [25] M. J. Piotrowski, C. G. Ungureanu, P. Tereshchuk, K. E. A. Batista, A. S. Chaves, D. Guedes-Sobrinho, J. L. F. Da Silva, *J. Phys. Chem. C* **2016**, *120*, 28844-28856
- [26] R. Bader, *Atoms in Molecules: A Quantum Theory*. Oxford University Press, USA.
- [27] F. Viñes, A. Desikusumastuti, T. Staudt, A. Görling, J. Libuda, K. M. Neyman, *J. Phys. Chem. C* **2008**, *112*, 16539-16549.
- [28] F. Viñes, C. Loschen, F. Illas, K. M. Neyman, *J. Catal.* **2009**, *266*, 59-63.
- [29] F. Calle-Vallejo, J. I. Martínez, J. M. García-Lastra, P. Sautet, D. Loffreda, *Angew. Chem. Int. Ed.* **2014**, *53*, 8316-8319.
- [30] A. Notario-Estévez, S. M. Kozlov, F. Viñes, F. Illas, *Chem. Commun.* **2015**, *51*, 5602-5605.
- [31] L. Vega, B. Martínez, F. Viñes, F. Illas, *Phys. Chem. Chem. Phys.* **2018**, *20*, 20548-20554
- [32] G. Kresse, J. Furthmüller, *Phys. Rev. B* **1996**, *54*, 11169-11186.
- [33] J. P. Perdew, K. Burke, M. Ernzerhof, *Phys. Rev. Lett.* **1996**, *77*, 3865-3868.
- [34] L. Vega, J. Ruvireta, F. Viñes, F. Illas, *J. Chem. Theory Comput.* **2018**, *14*, 395-403
- [35] M. Methfessel, A. T. Paxton, *Phys. Rev. B* **1989**, *40*, 3616-3621.
- [36] P. Janthon, S. Luo, S. M. Kozlov, F. Viñes, J. Limtrakul, D. G. Truhlar, F. Illas, *J. Chem. Theory Comput.* **2014**, *10*, 3832-3839.
- [37] H. J. Monkhorst, J. D. Pack, *Phys. Rev. B* **1976**, *13*, 5188.
- [38] A. A. B. Padama, H. Kishi, R. L. Arevalo, J. L. V. Moreno, H. Kasai, M. Taniguchi, M. Uenishi, H. Tanaka, Y. Nishihata, *J. Phys.: Condens. Matter* **2012**, *24*, 175005.
- [39] Z.-H. Zeng, J. L. F. Da Silva, W.-X. Li, *Phys. Chem. Chem. Phys.* **2010**, *12*, 2459-2470.
- [40] J. Ruvireta, L. Vega, F. Viñes, *Surf. Sci.* **2017**, *664*, 45-49.